Quantitative Systems Pharmacology Model Predictions for Efficacy of Atezolizumab and Nab-Paclitaxel in Triple-Negative Breast Cancer

Hanwen Wang[1]*, Huilin Ma[1], Richard J. Sové[1], Leisha A. Emens[2], Aleksander S. Popel[1,3]

[1] Department of Biomedical Engineering, Johns Hopkins University School of Medicine, Baltimore, MD, USA
[2] University of Pittsburgh Medical Center, Hillman Cancer Center, Pittsburgh, PA, USA
[3] Department of Oncology, and the Sidney Kimmel Cancer Center, Johns Hopkins University School of Medicine, Baltimore, MD, USA

* Corresponding author
Address: 613 Traylor Bldg., 720 Rutland Avenue, Baltimore, MD 21205, USA
E-mail: hwang163@jhmi.edu

SUPPLEMENTARY MATERIALS

Supplementary Methods

Cancer Module

The tumor growth kinetics is modified from the logistic growth, as in our previous cancer module (*1*), to the Gompertzian growth proposed by *Hahnfeldt et al.* to introduce the dynamics of tumor vasculature growth (*2*). Since the tumor volume in our model is calculated by the total number of cancer cells in the tumor compartment, the modified cancer cell growth follows the equations:

$$\frac{dC_i}{dt} = -k_{C,growth} C_i \log\left(\frac{C_{total}}{C_{\max}}\right) - \left(k_{C,death} + k_{C,nabp} \frac{[NabP]}{[NabP] + EC50_{nabp}} f_{C,nabp} + k_{C,T} \frac{T}{T + K_{C,T} C_{total}} \frac{T}{T + K_{C,Treg} T_{reg}} (1 - H_{PD1})(1 - H_{TGF\beta})(1 - H_{MDSC}) \right) C_i$$

$$\frac{dC_{max}}{dt} = k_{K,g} C_{total} \frac{c_{vas}}{c_{vas} + EC50_{vas}} - k_{K,d} C_{max} (C_{total} V_{cell})^{\frac{2}{3}} - k_{K,nabp} C_{max} [NabP]$$

The first equation describes the dynamics of cancer cells in each cancer clone, C_i, added by a cancer module. The first term describes the cancer cell proliferation with the proliferation rate, $k_{C,growth}$, the total number of cancer cells in all cancer clones, C_{total}, and the maximal capacity of cancer cells in the tumor, C_{max}, which is adapted from *Hahnfeldt et al.* (*2*). The second term describes the death of cancer cells due to apoptosis, nab-paclitaxel, and effector T cell (Teff). Apoptosis, which is caused by natural cell death or natural killer cells, is assumed to be a first-order reaction with a rate constant, $k_{C,death}$. Cytotoxic activity by nab-paclitaxel is incorporated with a rate constant, $k_{C,nabp}$, a Hill function representing the intrinsic and acquired resistance of cancer cells to nab-paclitaxel with varying effective concentration, $EC50_{nabp}$, and a fraction of

cancer cells that is accessible by nab-paclitaxel, $f_{C,nabp}$. Cancer cell killing by Teff are calculated by the maximal killing rate, $k_{C,T}$, the ratio of Teff and C_{total}, the ratio of Teff and regulatory T cell (Treg), and the Hill functions representing the inhibitory effects of PD-1, TGF-β, and myeloid-derived suppressor cells (MDSCs) (*3*).

The second equation describes the dynamics of the maximal number of cancer cells that can be supported by the tumor vasculature. The first term reflects the growth of tumor capacity by angiogenic factors, such as VEGF-A, with the baseline growth rate, $k_{K,g}$, the intratumoral concentration of angiogenic factors, c_{vas}, and the effective concentration of angiogenic factors on tumor vasculature growth, $EC50_{vas}$. The second term represents the endogenous inhibition of existing tumor vasculature, such as death of endothelial cells, with a degradation rate, $k_{K,d}$ (*2*). The third term represents the death of endothelial cells by nab-paclitaxel, with a dose dependent rate, $k_{K,nabp}$ (*4*). The parameters related to the tumor growth are assumed to follow lognormal distributions, and their ranges are fitted to *in vivo* tumor growth data from breast cancer mouse model. The simulated tumor growth is plotted with 60% and 90% confidence intervals and the data from *Desai et al.* in Figure S6 (*5*). The estimated parameters are then scaled up to human using equation: $\theta_{human} = \theta_{mice}\left(\frac{WT_{mice}}{WT_{human}}\right)^{\frac{1}{4}}$ (*6*).

Tumor volume (tumor compartment capacity) is calculated by the equation as follows:

$$V_T = (V_{cancer\_cell} * C_{total} + V_{T\_cell} * T_{total})/V_e$$

Here, V_{cancer_cell} and V_{T_cell} are the volumes of a single cancer cell and a single T cell, respectively, which are estimated by the diameter of breast cancer cells and T cells. T_{total} represents the total number of Teff, Treg, and $CD4^+$ helper T cells (Th) in the tumor, including exhausted T cells, and V_e is the volume fraction of the intracellular space in breast tumors. Tumor diameter and percentage change from baseline are calculated, assuming a spherical tumor, by the equation as follows:

$$D_T = 2\left(\frac{3}{4\pi}V_T\right)^{\frac{1}{3}}$$

$$D_{T,perc} = \left(\frac{D_T - D_T^0}{D_T^0}\right) * 100\%$$

Here, D_T is the tumor diameter, $D_{T,perc}$ is the percentage change from baseline, and D_T^0 is the initial tumor diameter. During each model initialization, a desired tumor diameter is inputted to represent the pre-treatment tumor size for a virtual patient. Then, the model is simulated starting from a small number of cancer cells until the tumor volume reaches the desired pre-treatment tumor size. The amount of species and parameter values at that time point are saved and used as the initial (pre-treatment) condition for the virtual patient. At the post-processing step, $D_{T,perc}$ is calculated for each virtual patient for efficacy prediction based on RECIST 1.1 (*7*).

T cell Modules (Teff, Treg, and Th)

Naïve T Cell Dynamics

Dynamics of naïve T cells are incorporated into the central, peripheral, and tumor compartments. Although experimental and clinical studies of breast cancer confirm the naïve T cell infiltration and activation in the tumor, we assume that the naïve T cell activation in the tumor is negligible comparing to that in the tumor-draining lymph nodes (*8*). The naïve T cell dynamics are modeled as follows:

$$\frac{d}{dt}[nT]_C = \theta - Q_{nT,P,in}[nT]_C + Q_{nT,P,out}[nT]_P - Q_{nT,LN,in}[nT]_C + Q_{nT,LN,out}[nT]_{LN} - k_{nT,death}[nT]_C$$

$$\frac{d}{dt}[nT]_P = k_{nT,pro}\frac{[nT]_P}{[nT]_P + K_{nT,pro}} + Q_{nT,P,in}[nT]_C - Q_{nT,P,out}[nT]_P - k_{nT,death}[nT]_P$$

$$\frac{d}{dt}[nT]_{LN} = k_{nT,pro}\frac{[nT]_{LN}}{[nT]_{LN} + K_{nT,pro}} + Q_{nT,LN,in}[nT]_C - Q_{nT,LN,out}[nT]_{LN} - k_{nT,death}[nT]_{LN} - k_{act}H_{APC}H_{Ag}[nT]_{LN}$$

Here, $[nT]_i$ represents the average number of naïve $CD4^+$/$CD8^+$ T cell of a single clonotype in the corresponding compartment, whose initial amount is calculated by dividing the absolute number of naïve T cells measured from healthy individuals by the T cell clonotype diversity (*9, 10*). θ represents zero-order thymic export of naïve T cells, which is estimated by the average ages of patients with breast cancer at diagnosis (*11-13*). The transport of naïve T cells among the four compartments are based on the model by *Zhu et al.* and are estimated to keep the naïve T cell densities at the initial conditions when tumor is not present (thus no naïve T cell activation by tumor antigens) (*9, 14*). Since the naïve T cell densities are sustained mainly by the proliferation in peripheral lymphoid organs, the proliferation rate is estimated based on the *in vivo* data reported by *Braber et al.* (*15*).

T Cell Activation and Homing

The activation of naïve T cell in the tumor-draining lymph nodes depends on the number of available binding sites and T cell receptor (TCR)–peptide-MHC (pMHC) complexes on the surface of mature antigen-presenting cells (mAPCs), which are implemented as Hill functions named H_{APC} and H_{Ag}, respectively. The activation is thus guided by the equations:

$$\frac{d}{dt}[aT]_{LN} = k_{act}H_{APC}H_{Ag}[nT]_{LN}n_{T,clones} - \frac{k_{T,pro}}{N_{aT}}[aT]_{LN}$$

$$\frac{dT_{LN}}{dt} = \frac{k_{T,pro}}{N_{aT}}2^{N_{aT}}[aT]_{LN} - Q_{T,LN,out}T_{LN} - k_{T,death}T_{LN}$$

Here, $[aT]_{LN}$ represents the activated T cells in TDLNs, and T_{LN} represents the final forms of activated T cell (i.e. Teff, Treg, and Th) that are eventually transported into the tumor. Since

$[nT]_{LN}$ represents the number of naïve T cells of a single clonotype, the first term is multiplied by the number of corresponding antigen-specific T cell clones, $n_{T,clones}$, to calculate the total number of activated T cells that can recognize tumor neoantigen (i.e. Teff and Th) or tumor-associated self-antigen (i.e. Treg). Thus, the numbers of neoantigen-specific and self-antigen-specific T cell clones are scalar parameters, which were estimated by the number of nonsynonymous mutations in TNBC (*16*). k_{act} is the maximal activation rate of naïve T cell by mAPC, $k_{T,pro}$ is the proliferation rate of activated T cell, and N_{aT} is the total number of divisions that an activated T cell can undergo while transitioning to its final form (*17*). N_{aT} is calculated using the equation:

$$N_{aT} = N_{TCR} + N_{costim}H_{CD28} + N_{IL2}H_{IL2}$$

where N_{TCR}, N_{costim}, and N_{IL2} represent the number of cell divisions by signals from TCR, costimuli on mAPC, and IL-2 secreted by activated $CD4^+$ helper T cell, respectively. According to the data from *Marchingo et al.*, the effect of the three signals on activated T cell expansion can be predicted by the linear sum of the underlying signal components (*17*).

The transport of activated T cells is based on the model by *Zhu et al.*, and is described by the equations:

$$\frac{dT_C}{dt} = Q_{T,LN,out}T_{LN} - Q_{T,P,in}T_C + Q_{T,P,out}T_P - Q_{T,T,in}T_C\frac{C_{total}^2}{C_{total}^2 + K_{C,rec}} - k_{T,death}T_C$$

$$\frac{dT_P}{dt} = Q_{T,P,in}T_C - Q_{T,P,out}T_P - k_{T,death}T_P$$

$$\frac{dT_T}{dt} = Q_{T,T,in}T_C\frac{C_{total}^2}{C_{total}^2 + K_{C,rec}} - k_{T,death}T_T$$

Notably, the tumor-infiltrating T cells, T_T, have additional dynamics for Teff, which follows the equation:

$$\frac{dT_T}{dt} = Q_{T,T,in}T_C\frac{C_{total}^2}{C_{total}^2 + K_{C,rec}} - (k_{T,death} + k_{Treg}\frac{T_{reg}}{T_T + T_{reg}} + k_{Tcell}\frac{C_{total}}{C_{total} + T_T}H_{PD1})T_T$$

The additional terms represent the Teff inhibition by Treg and tumor cell, respectively. H_{PD1} represent the inhibitory effect of PD1-PDL1/2 interactions between Teff and tumor cell.

Antigen-Presenting Cell Module

The APC and antigen modules describe the APC recruitment into the tumor compartment, APC maturation, and mature APC transport to the tumor-draining lymph nodes compartment. The dynamics of APCs is described as follows:

$$\frac{d[APC]_T}{dt} = k_{APC,death}(\rho_{APC}V_T - [APC]_T) - k_{APC,mat}\frac{c}{c + c_{50}}[APC]_T$$

$$\frac{d[APC]_{LN}}{dt} = k_{APC,death}(\rho_{APC}V_{LN} - [APC]_{LN})$$

$$\frac{d[mAPC]_T}{dt} = k_{APC,mat}\frac{c}{c+c_{50}}[APC]_T - k_{APC,mig}[mAPC]_T - k_{mAPC,death}[mAPC]_T$$

$$\frac{d[mAPC]_{LN}}{dt} = k_{APC,mig}[mAPC]_T - k_{mAPC,death}[mAPC]_{LN}$$

Here, $k_{APC,death}$ is the entry/death rate of APCs; ρ_{APC} is the baseline APC density; $k_{APC,mat}$ is the maturation rate that depends on the concentration of maturation signals, c; $k_{APC,mig}$ is the migration rate of mAPC from tumor to the TDLNs; and $k_{mAPC,death}$ is the death rate of mAPC. The maturation signals are assumed to be released with the same rate as cancer cell death by apoptosis and Teffs (*18-20*).

The number of mAPCs in the TDLNs is used to calculate the Hill function, H_{APC}, which is implemented in the T cell module above. It is calculated using equation:

$$H_{APC} = \frac{n_{sites,APC}[mAPC]_{LN}}{n_{sites,APC}[mAPC]_{LN} + n_{T,clones}[nT]_{LN}}$$

The equation above is different based on the final form of the T cell activation. For $CD8^+$ naïve T cell, $n_{T,clones}$ represents the number of neoantigen clones, which is assumed to be equal to the number of tumor-specific T cell clones for Teff activation. For $CD4^+$ naïve T cell, $n_{T,clones}$ represent the number of neoantigen clones and self-antigen clones for Th and Treg activation, respectively. The fate of $CD4^+$ naïve T cells is thus dependent on the number of neoepitopes and self-epitopes on the surface of mAPCs, as well as the transdifferentiation from Th to Treg mediated by TGF-β (*21*).

Antigen Module

The mechanisms of antigen processing and presentation are adapted from several well-established models (*18-20*). Tumor neoantigen and tumor-associated self-antigen are released upon death of cancer cells and are internalized into intracellular vesicles of APCs, where they are processed into short peptides. The peptides then bind with MHC molecules based on their binding affinity, and the pMHC complexes are presented on the cell surface to be recognized by the antigen-specific T cell receptors. The various forms of antigen during this process are governed by the equations:

$$V_e\frac{dP_e}{dt} = k_{up}P_TV_e - k_{P,deg}P_eV_e$$

$$V_e\frac{dp_e}{dt} = k_{P,deg}P_eV_e - k_{p,deg}p_eV_e - k_{on}M_ep_eA_e + k_{off}[Mp]_eA_e$$

$$A_e\frac{d[Mp]_e}{dt} = k_{on}M_ep_eA_e - k_{off}[Mp]_eA_e - k_{out}[Mp]_eA_e$$

$$A_s\frac{d[Mp]_s}{dt} = k_{out}[Mp]_eA_e - k_{off}[Mp]_sA_s$$

$$A_e\frac{dM_e}{dt} = k_{off}[Mp]_eA_e - k_{on}M_ep_eA_e - k_{out}M_eA_e + k_{in}M_sA_s$$

$$A_s \frac{dM_s}{dt} = k_{off}[Mp]_s A_s - k_{in} M_s A_s + k_{out} M_e A_e$$

Here, P_i, p_i, M_i, and $[Mp]_i$ represent the concentration of the antigen, the peptide, the MHC molecule, and the pMHC complexes, respectively. V_i and A_i represent the volume and the surface area, respectively. The subscripts *e* and *s* represent APC endosomal and surface compartment, respectively. The antigen uptake rate, k_{up}, antigen degradation rate, $k_{P,deg}$, peptide degradation rate, $k_{p,deg}$, peptide-MHC association rate, k_{on}, dissociation rate, k_{off}, exocytosis rate of pMHC complexes, k_{out}, and internalization rate of MHC molecules, k_{in}, were estimated by *Chen et al.* (*18*). The above equations are used for both tumor-associated self-antigens and tumor neoantigen clones. We assume that the number of pMHC complexes on cell surface depends on the antigen concentration in the tumor during the migration of mAPC to the TDLNs (*22*).

The concentration of pMHC complex is used to calculate the total number of the TCR-pMHC binding between tumor-specific naïve T cells and mAPCs, which determines the Hill function H_{Ag} in the equations for T cell activation. The equations involved are shown:

$$[TCR\_MHC]_{tot} = \frac{1}{2}\left(\frac{[Mp]_s}{n_{T,clones}} + TCR_{tot} + K_{D,TCR} - \sqrt{\left(\frac{[Mp]_s}{n_{T,clones}} + TCR_{tot} + K_{D,TCR}\right)^2 - 4\frac{[Mp]_s}{n_{T,clones}} TCR\_tot}\right)$$

$$[TCR]_{active} = \frac{k_{off,TCR}}{k_{off,TCR} + \phi_{TCR}}\left(\frac{k_{p,TCR}}{k_{p,TCR} + k_{off,TCR}}\right)^{N_{TCR}} [TCR\_MHC]_{tot}$$

Here, $[TCR\_MHC]_{tot}$ is the total number of TCR-pMHC complexes, and $[TCR]_{active}$ is the number of active TCRs. $[Mp]_s$ is divided by the number of tumor-specific T cell clones to represent the number of pMHC complexes of a single clonotype. This is based on the model assumption that each TCR clone can recognize one antigen clone, and each antigen clone can be recognized by one TCR clone. TCR_{tot} is the total number of TCR on T cells; $K_{D,TCR}$ is the binding affinity between TCR and pMHC complex with dissociation rate of $k_{off,TCR}$; $k_{p,TCR}$ is the modification rate of TCR-pMHC complexes; ϕ_{TCR} is the modification rate of TCR-pMHC complexes to the non-signaling state; and N_{TCR} is the number of modification steps. The number of active TCRs determines the Hill function, H_{Ag}, for naïve T cell activation.

$$H_{Ag} = \frac{[TCR]_{active}}{[TCR]_{active} + K_p}$$

K_p is the half-maximal active TCR level for naïve T cell activation.

Pharmacokinetic Module (for Checkpoint Inhibitors)

Similarly to the methods reported in our previous studies (*23*), the permeability of the antibody between the peripheral tissues and capillaries can be estimated by its Stokes-Einstein radius, which is calculated via the equation by *Venturoli et al.*: $a_e = 0.483 * (MW)^{0.386}$ (*24*). Since atezolizumab has a molecular weight of 145 kDa, it has a Stokes-Einstein radius of 47.4 Å. The calculated radius is used to determine the theoretical permeability-surface area product as 1.5e-4 mL/(s*100g) (*25*). Using a surface area of 70 cm^2/g, the theoretical permeability of atezolizumab between the central and the peripheral compartments is calculated to be 2e-8 cm/s, which is used as the starting value for fitting. The permeability of antibody between the central and the tumor compartments is estimated to be 3e-7 cm/s according to multiple literature evidence (*26, 27*), and the surface area is estimated to be 28.4 cm^2/cm^3 (*27*).

The clearance rate, the permeability between the central and the peripheral compartments, and the volume fractions of the plasma (in the central compartment) and the interstitial space (in the peripheral compartment) available to atezolizumab are fitted to the clinical measurements from *Stroh et al.* (*28*), as shown in Figure S7. The equations that govern the antibody transport are shown:

$$V_C \frac{d[A]_C}{dt} = k_{CP} SA_{CP} \left(\frac{[A]_P}{\gamma_P} - \frac{[A]_C}{\gamma_C} \right) + k_{CLN} SA_{CLN} \left(\frac{[A]_{LN}}{\gamma_{LN}} - \frac{[A]_C}{\gamma_C} \right) + k_{CT} SA_{CT} \left(\frac{[A]_T}{\gamma_T} - \frac{[A]_C}{\gamma_C} \right) + \frac{Q_{LD}[A]_{LN}}{\gamma_{LN}} - k_{cl}[A]_C V_C$$

$$V_P \frac{d[A]_P}{dt} = -k_{CP} SA_{CP} \left(\frac{[A]_P}{\gamma_P} - \frac{[A]_C}{\gamma_C} \right)$$

$$V_T \frac{d[A]_T}{dt} = -k_{CT} SA_{CT} \left(\frac{[A]_T}{\gamma_T} - \frac{[A]_C}{\gamma_C} \right) - \frac{Q_{LD}[A]_T}{\gamma_T}$$

$$V_{LN} \frac{d[A]_{LN}}{dt} = -k_{CLN} SA_{CLN} \left(\frac{[A]_{LN}}{\gamma_{LN}} - \frac{[A]_C}{\gamma_C} \right) + \frac{Q_{LD}[A]_T}{\gamma_T} - \frac{Q_{LD}[A]_{LN}}{\gamma_{LN}}$$

Here, $[A]_i$ is the antibody concentration, V_i is the compartment volume, k_{ij} is the permeability between compartment *i* and *j*, SA_{ij} is the total surface area of endothelial cells at the interface of compartment *i* and *j*, γ_i is volume fraction of interstitial space available to the antibody, k_{cl} is clearance rate, and Q_{LD} is the rate of lymphatic drainage, from the tumor, to TDLNs, to the central compartment. Subscripts *C, P, LN, T* represent the central, peripheral, TDLNs, and tumor compartments, respectively.

The drug administration is performed by creating a SimBiology dose object, which contains the amount of the doses, the infusion times, and the dose schedules. Since the dose object is used as an input when simulating the SimBiology model, the dose information is not saved in the SBML code but can be found in the MATLAB scripts. The default dose regimens for atezolizumab and

nab-paclitaxel are 1200 mg Q3W and 100 mg/m^2 Q3/4W, respectively, and can be modified in the *in silico* virtual clinical trial script.

Checkpoint Module

Dynamics of PD-L1-related checkpoint molecules

Dynamics of PD-1, PD-L1, CD80, and anti-PD-(L)1 antibody are adapted from the model by *Cheng et al.* (*29*), and simplified by *Jafarnejad et al.* (*22*). The interactions between the ligands and receptors occur in a model sub-compartment that represents the immunological synapse. We assume that the ligands and receptors are evenly distributed on the cell surface so that their densities in the synapse are calculated by dividing their expression levels by the total cell surface area. According to *Jafarnejad et al.*, the explicit representation of the diffusive entry of surface molecules to the synapse is negligible due to its rapid dynamics. Instead, the area of the synapse is increased by a factor of 3 to account for the effect of diffusion (*22*).

The numbers of checkpoint molecules on cells are estimated based on measurements using quantitative flow cytometry with fluorescent beads (*29*), which were then scaled up based on the PD-1 measurements by *Mkrtichyan et al.* (*30*) to account for possible underestimation of PD-L1/2 from QuantiBRITE bead measurements. These parameters are varied in a wide range in the virtual patient generation to account for the uncertainty and inter-individual variability. The interactions among checkpoint molecules and the PD-L1 inhibitor, atezolizumab, are described by a bivalent model using equations:

$$\frac{d[PD1\_PDL1]}{dt} = \frac{k_{on,PD1\_PDL1}}{d_{syn}}[PD1][PDL1] - k_{off,PD1\_PDL1}[PD1\_PDL1]$$

$$\frac{d[PD1\_PDL2]}{dt} = \frac{k_{on,PD1\_PDL2}}{d_{syn}}[PD1][PDL2] - k_{off,PD1\_PDL2}[PD1\_PDL2]$$

$$\frac{d[PDL1\_atezo]}{dt} = 2k_{on,PDL1\_atezo}[PDL1]\frac{[atezo]}{\gamma_T} - k_{off,PDL1\_atezo}[PDL1\_atezo] - \chi_{atezo}\frac{k_{on,PDL1\_atezo}}{d_{syn}N_A}[PDL1\_atezo][PDL1] + 2k_{off,PDL1\_atezo}[PDL1\_atezo\_PDL1]$$

$$\frac{d[PDL1\_atezo\_PDL1]}{dt} = \chi_{atezo}\frac{k_{on,PDL1\_atezo}}{d_{syn}N_A}[PDL1\_atezo][PDL1] - 2k_{off,PDL1\_atezo}[PDL1\_atezo\_PDL1]$$

$$\frac{d[PDL1]}{dt} = k_{out,PDL1}\frac{[IFN\gamma]}{[IFN\gamma]+EC50_{IFNg}}\left(1-\frac{[PDL1]_{total}}{r_{PDL1,IFN}[PDL1]_{baseline}}\right)$$
$$+ k_{in,PDL1}([PDL1]_{baseline}-[PDL1]_{total}) - \frac{k_{on,PD1\_PDL1}}{d_{syn}}[PD1][PDL1]$$
$$+ k_{off,PD1\_PDL1}[PD1\_PDL1] - 2k_{on,PDL1\_atezo}[PDL1]\frac{[atezo]_T}{\gamma_T}$$
$$+ k_{off,PDL1\_atezo}[PDL1\_atezo] - \chi_{atezo}\frac{k_{on,PDL1\_atezo}}{d_{syn}N_A}[PDL1\_atezo][PDL1]$$
$$+ 2k_{off,PDL1\_atezo}[PDL1\_atezo\_PDL1]$$

Here, the model species represent the 2-D densities of the checkpoint molecules in the synapse. k_{on} and k_{off} are the association and dissociation rates of checkpoint interactions; the 2s as coefficients for k_{on} and k_{off} of antibodies represent the stochiometric corrections due to antibody bivalency (*31*); γ_T is the volume fraction of tumor interstitium that is available to the antibody; χ_{atezo} is the intrinsic antibody cross-arm binding efficiency (*31*); the denominator, d_{syn}, is the thickness of the confinement space between two cells during the interaction, which aims to transfer the 3-D binding affinity to 2-D; N_A is Avogadro's number. $k_{out,PDL1}$ is the expression rate of PD-L1 by IFNγ; $r_{PDL1,IFN}$ is the number of folds increase of PD-L1 expression from baseline level by IFNγ; $k_{in,PDL1}$ is the degradation/internalization rate of unbound PD-L1 molecules (*32*). The number of bound PD-1 molecules to PD-L1/2 molecules in the tumor determines the Hill function, H_{PD1}, for inhibitory effects of Treg and cancer cell on Teff.

Dynamics of CTLA-4-related checkpoint molecules

Dynamics of CTLA-4, CD28, CD80/86, and anti-CTLA-4 antibody are based on the model by *Jansson et al.* (*33*) and are described using similar methods above. Briefly, CD28 and CTLA-4 on naïve T cells bind to CD80 and CD86 on APCs, and PD-L1 on T cells binds to CD80 on APCs to compete with CD28 in tumor-draining lymph nodes (*34*). CD28 is a co-stimulatory signal that enhances the naïve T cell activation by increasing the number of T cell divisions. Since CTLA-4 outcompetes CD28 due to its higher binding affinity to CD80/CD86, the blockade of CTLA-4 restores ligand availability for CD28 that leads to enhanced T cell activation and proliferation. Similar to PD-L1-related dynamics, the model includes stochiometric corrections for antibody bivalency and dimerization of CTLA-4 and CD86 on cell surface which also results in bivalency (*31, 35, 36*). The number of bound CD28 molecules to CD80/86 molecules on mAPCs determines the Hill function, H_{CD28}, to calculate the number of T cell divisions by costimulatory signals.

Overall, the checkpoint module is called twice to simulate the immunological synapse between T cells and mAPCs during naïve T cell activation in the lymph nodes and that between T cells and tumor cells or immune cells in the tumor (e.g. cancer cells, fibroblasts, MDSCs, and macrophages). Since the absolute numbers of checkpoint molecules on tumor and immune cells are not available from literature, their expressions are estimated based on the corresponding *in vitro* measurements on mature dendritic cells (*29, 30, 33*). Moreover, the number of PD-L1 molecules in the model represents its average expression level on all tumor/immune cells in the

tumor compartment, so that the calculated Hill function, H_{PD1}, represents the overall effect of PD-1/PD-L1 interactions in the tumor.

Myeloid-Derived Suppressor Cell (MDSC) Module

As introduced in the previous study, MDSC module describes the MDSC recruitment into the tumor compartment, arginase-I (Arg-I) and nitric oxide (NO) secretion, and Teff inhibition and Treg expansion mediated by Arg-I and/or NO (*1*). MDSC recruitment is mediated by CCL2 secreted by cancer cells in addition to a baseline recruitment rate, using the following equation:

$$\frac{d[MDSC]}{dt} = (k_{brec,MDSC} + k_{rec,MDSC}\frac{[CCL2]}{[CCL2] + K_{CCL2,rec}})\left(\rho_{MDSC,max}V_T - [MDSC]\right)$$

Here, $k_{brec,MDSC}$ and $k_{rec,MDSC}$ represent the baseline recruitment rate and the maximal recruitment rate by CCL2, respectively; $K_{CCL2,rec}$ represents the EC50 of CCL2 on MDSC recruitment; and $\rho_{MDSC,max}$ represents the maximal MDSC density that varies among patients (*37*). The predicted CCL2 expression and migration indices are fitted to TNBC data (*1, 38, 39*). The major immunosuppressive factors secreted by MDSCs are assumed to be Arg-I and NO, whose expression rates are estimated based on *in vitro* experiments on breast cancer cells (*1, 40*). Since only the enzymatic activity of Arg-I is measured in enzyme unit, mU, we use mU as a placeholder of Arg-I concentration in the model, assuming that the protein concentration is proportional to the enzymatic activity. The unit of its production rate is then set to be mU*(microliter)/cell/day to estimate the amount of Arg-I produced by MDSCs per day. The units of production rates of NO and CCL2 are set to be nanomole/cell/day. While both Arg-I and NO inhibit cytotoxic killing of cancer cells by Teff, only Arg-I facilitates Treg expansion in the tumor (*40*). The effective concentrations are estimated based on *in vitro* experiments and listed in Supplementary Table S4 with references.

Nab-Paclitaxel Module

Pharmacokinetics

The plasma concentrations of nab-paclitaxel are simulated using a published 3-compartment PK model which is calibrated by clinical measurements from eight clinical trials involving patients with advanced or metastatic solid tumors (*41*). The intratumoral concentrations of nab-paclitaxel are then estimated by tumor-to-plasma ratio measured in *in vivo* studies using nab-paclitaxel in breast cancer mouse model (*42, 43*). The PK parameters and body surface area are varied within the 95% confidence interval reported by *Chen et al.* to represent the inter-individual variability (*41*). Tumor-to-plasma ratio of nab-paclitaxel is also varied for global uncertainty and sensitivity analysis (Figure S4).

Pharmacodynamics

The nab-paclitaxel module incorporates both cytotoxic and pro-angiogenic activities of nab-paclitaxel in this model. While the cytotoxic effect of nab-paclitaxel on cancer cells is well-established by *in vitro* and *in vivo* data from breast cancer mouse models, one of the challenges in chemotherapy is the development of chemo-resistance in the patients, which can be characterized into two types: intrinsic and acquired (*44*). Intrinsic chemo-resistance is caused by pre-existing mechanisms before the therapy begins, while the acquired chemo-resistance appears

during the therapy, both of which may be dependent on the cancer type and the chemotherapeutic agent (*45*). As a result, EC50s of nab-paclitaxel on breast cancer cells can be different among the patients and changing over time. To account for the intrinsic chemo-resistance, the module starts by randomly assigning an EC50 value of nab-paclitaxel to the initial cancer clone, which is added by the cancer module. The range of the initial EC50 of nab-paclitaxel is estimated using *in vitro* data from TNBC cell lines in the Genomics of Drug Sensitivity in Cancer (GDSC) database developed by *Yang et al.* (*46*). Besides the intrinsic resistance, the module further introduces a resistant cancer clone, on which the initially assigned EC50 value of nab-paclitaxel is increased by up to 100-fold, to represent the acquired chemo-resistance (*47, 48*). The development of the acquired chemo-resistance from the initial cancer clone to the resistant clone is simplified as a first-order reaction. The rate of the resistance development is estimated to capture the duration of response reported by the clinical trial. As shown in the Kaplan–Meier curve for duration of response (Figure S2), the model prediction matches the clinical results after calibration. Further, the resistant cancer clones may have slight changes in their proliferation rates, which is reported by *in vivo* studies (*49, 50*). In addition to its cytotoxic activity, nab-paclitaxel is reported to increase VEGF-A expression at low concentration, and thus lead to a pro-angiogenic effect on tumor vasculatures, which is implemented as described in the modified cancer module (*5, 51, 52*). At high concentration, nab-paclitaxel induces endothelial cell death with a dose-dependent rate estimated by *Mollard et al.* (*4*).

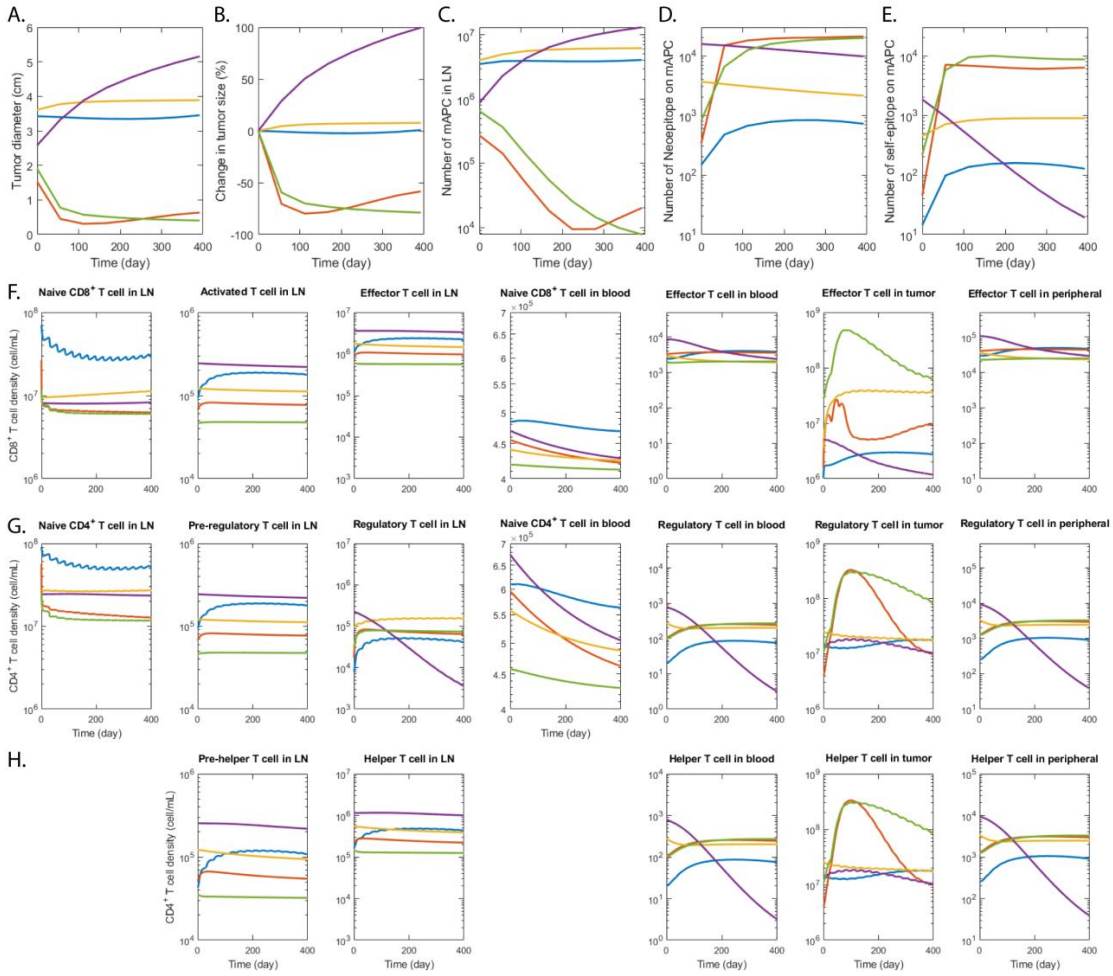

Figure S1. Sample Time Profiles in Combination Therapy of Nab-paclitaxel and Atezolizumab for 5 Virtual Patients Predicted by the QSP Model. Simulated data are plotted every 8 weeks, corresponding to the frequency of tumor measurements in the clinical trial. Tumor diameter (A), percentage change from baseline (B), number of mAPCs (C), neoepitope (D), and self-epitope (E), and densities of $CD8^+$ and $CD4^+$ T cells (F-H) in all compartments are plotted over 400 days. Each color represents the same virtual patient in all the subplots.

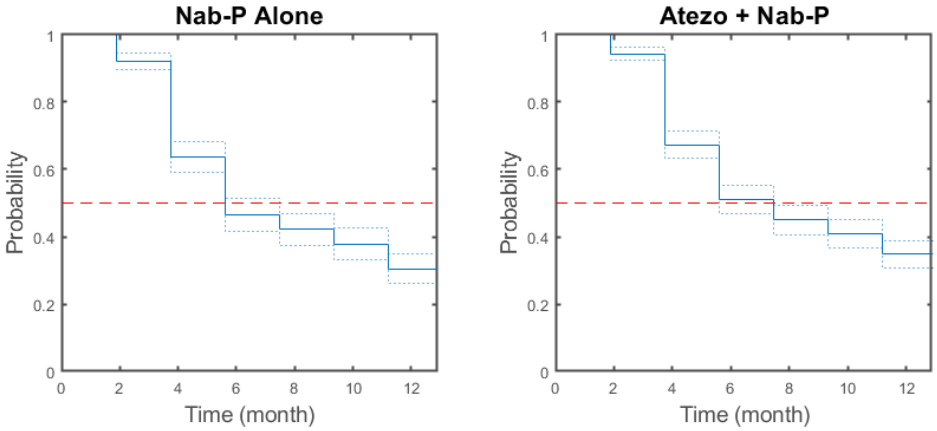

Figure S2. Kaplan-Meier Curve for Duration of Response. The predicted median durations of response for the nab-paclitaxel monotherapy and its combination with atezolizumab are 5.6 (95% confidence interval: 5.6-7.5) and 7.5 (5.6-9.3), respectively.

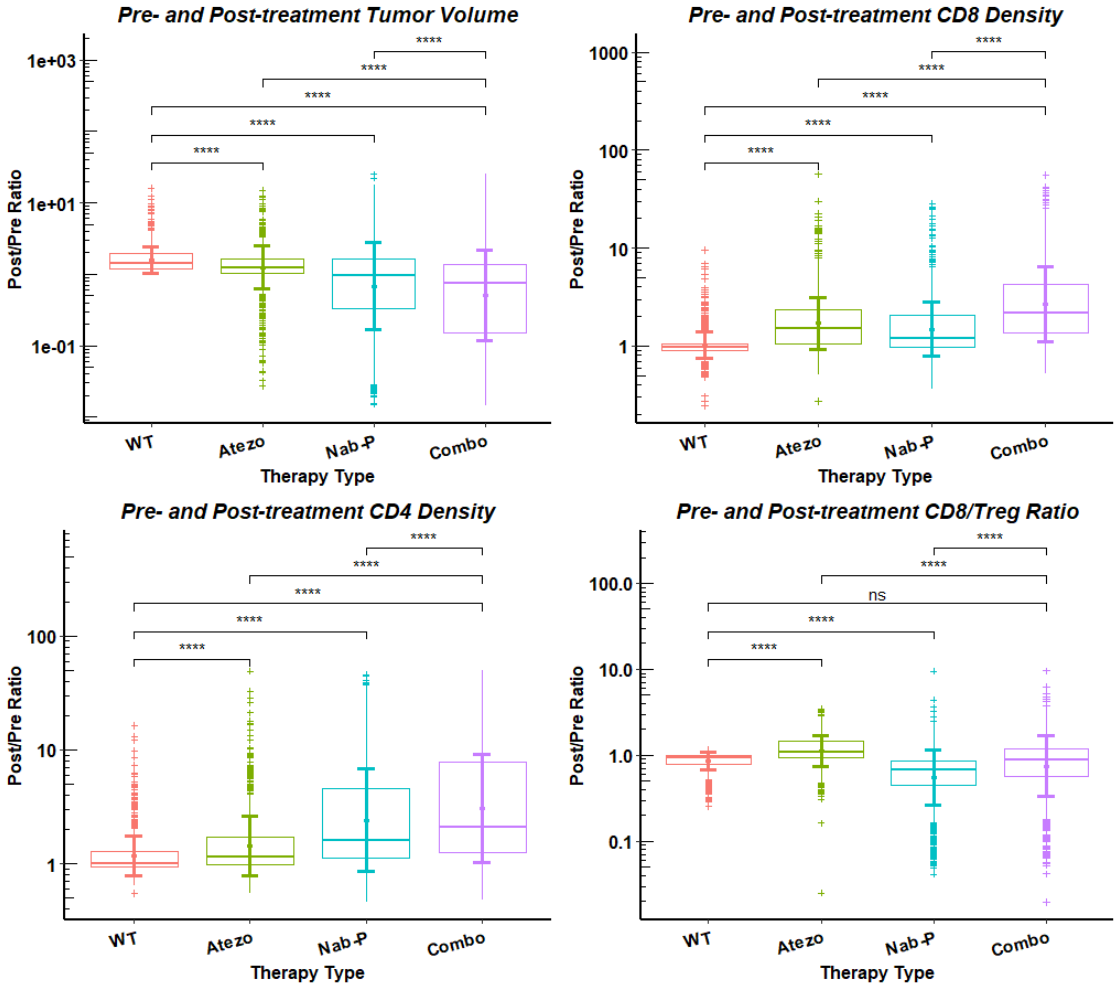

Figure S3. Changes of Biomarkers as Post- (week 8) to Pre-treatment Ratios in Various Therapy Types. Atezo, atezolizumab monotherapy 1200mg Q3W; Nab-P, nab-paclitaxel 100mg/m^2 Q3/4W; Combo, atezolizumab 840mg Q2W + nab-paclitaxel 100mg/m^2 Q3/4W. Statistical significance is calculated by Wilcoxon test.

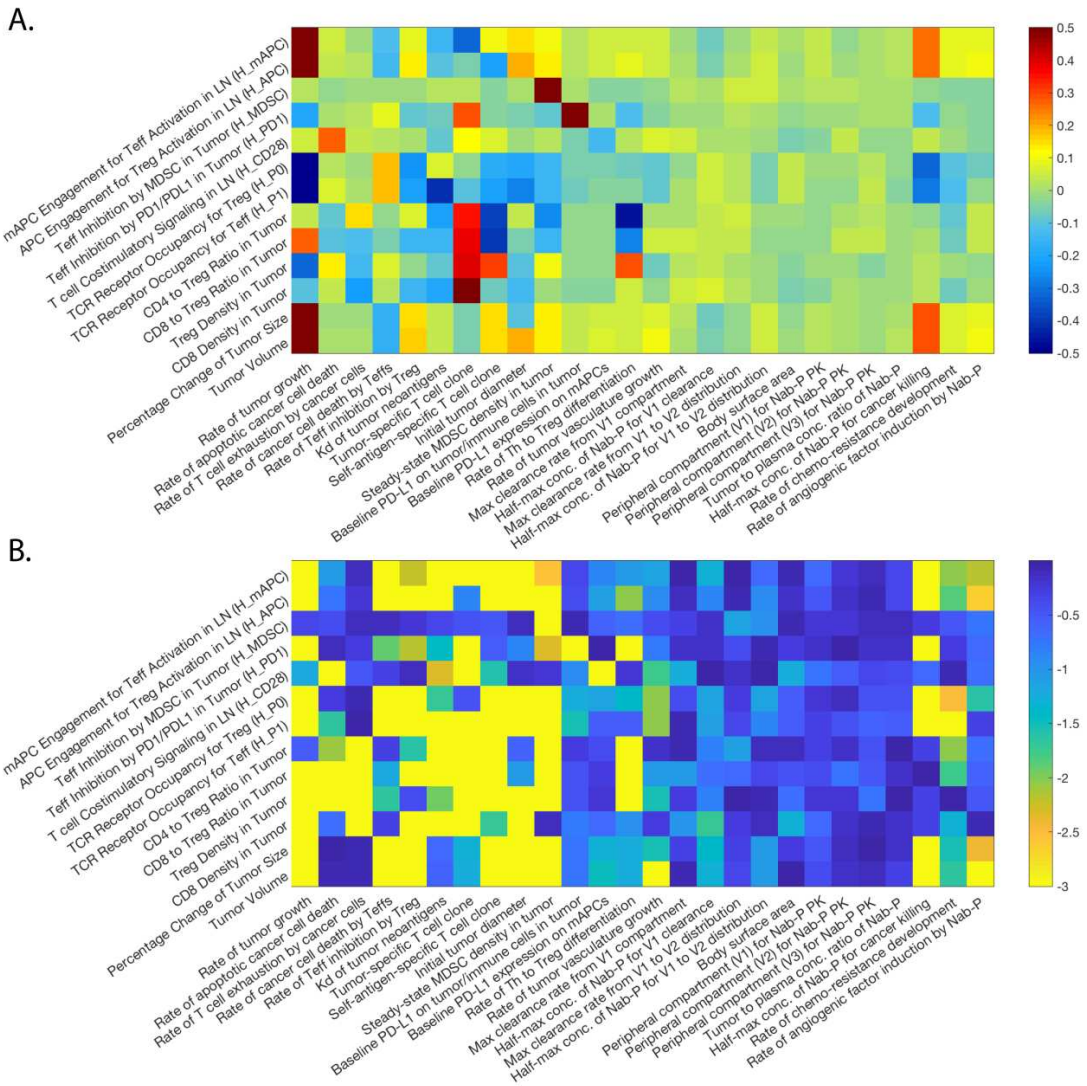

Figure S4. Global Uncertainty and Sensitivity Analysis. 26 parameters are assigned using Latin Hypercube Sampling (LHS) based on our estimated distribution. The Partial Rank Correlation Coefficient (PRCC) between selected post-treatment observations and input parameters (A) and the corresponding log10 p-values (B) are presented as a heatmap.

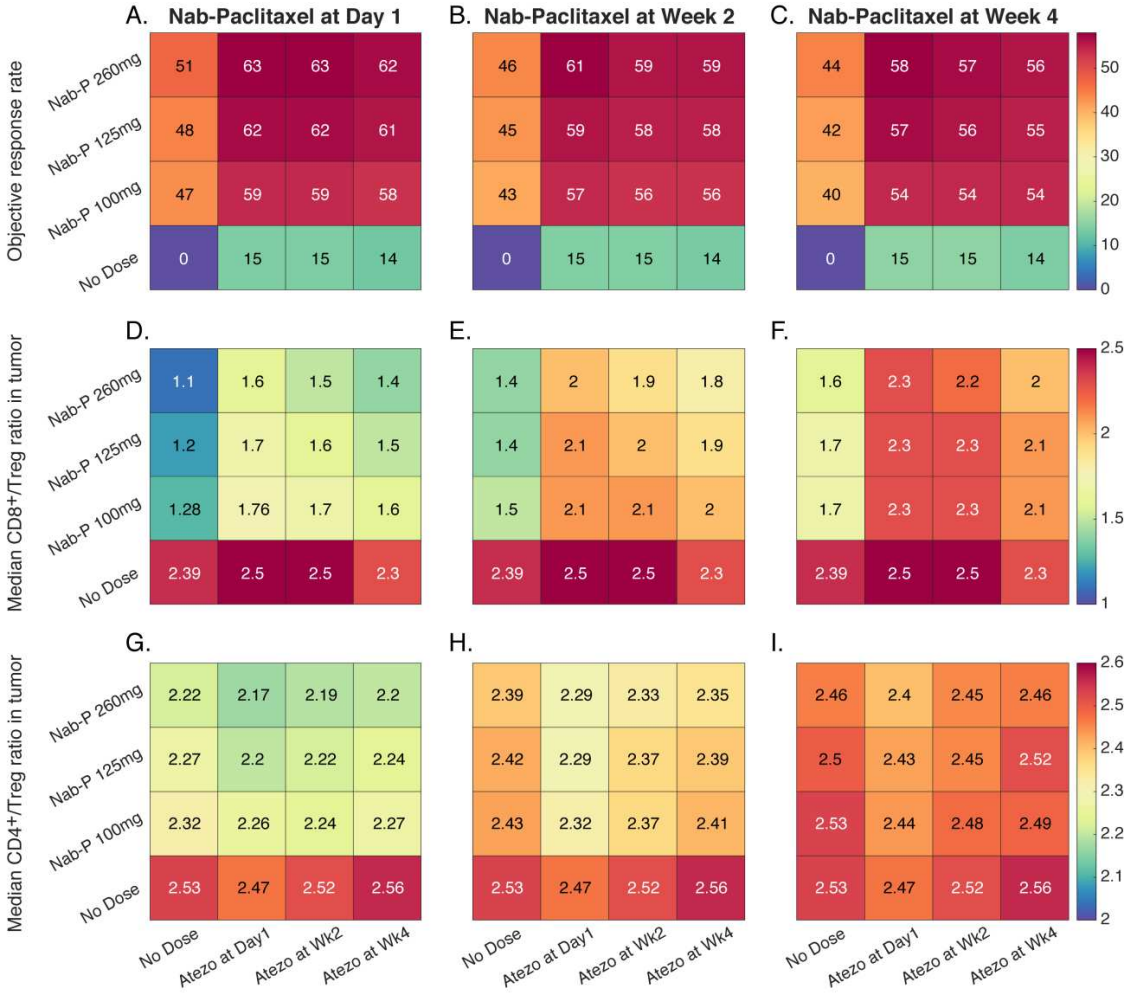

Figure S5. Model Simulation of Sequential Therapies using Various Nab-paclitaxel Doses and Schedules. Top row (A-C) represents the ORR of each dose regimen; middle row (D-F) represents the $CD8^+$/Treg ratio in the tumor at week 8; and bottom row (G-I) represents the $CD4^+$/Treg ratio in the tumor at week 8. Administration of nab-paclitaxel starts on day 1 (A,D,G), week 2 (B,E,H), and week 4 (C,F,I) upon reaching initial tumor diameter.

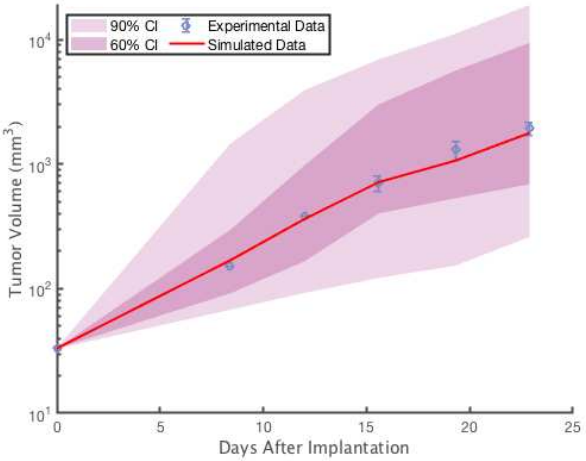

Figure S6. Tumor Volume vs. Time After Implantation. Experimental data are reported by *Desai et al.* using MX-1 xenograft mouse model. Tumor growth comparison starts at approximately 33mm^3, which corresponds to a 35mg tumor assuming a tumor density of 1.06kg/L.

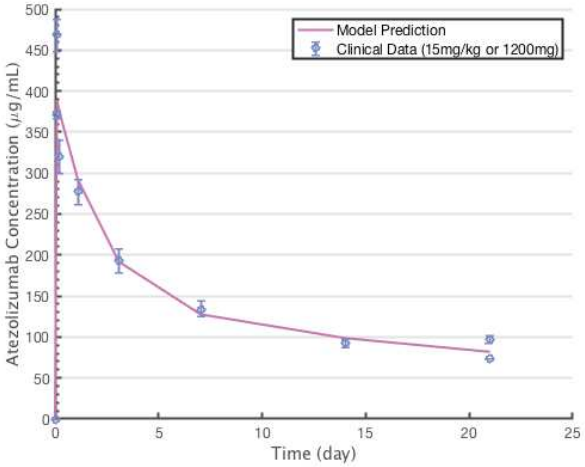

Figure S7. Plasma Concentration of Atezolizumab. Point data represent the plasma concentration measured after administration of 15 mg/kg or 1200 mg atezolizumab, as reported by *Stroh et al.* (*28*).

Table S1. Parameter Distribution and Range used in Virtual Patient Generation.

Parameter	Distribution	Geometric mean	Geometric standard deviation	Unit
Tumor Growth Rate	lognormal	0.0087	1	1/day
Rate of T cell killing of cancer cell		0.9	1	1/day
Binding affinity of neoantigen-MHC		27	1	nM
Neoantigen-specific T cell clone		63	0.7	dimensionless
Self-antigen-specific T cell clone		63	0.7	dimensionless
Initial tumor diameter		2.5	0.3	centimeter
Steady-state MDSC density		1.637e5	1	cell/mL
Rate of differentiation from Th to Treg		0.022	1	1/day
Half-max conc. of nab-paclitaxel for cancer killing		4.7e-8	1.1	molarity
Rate of chemo-resistance development		1e-4	1	1/day
Rate of angiogenic factor induction by nab-paclitaxel		0.017	1	picogram/cell/day
Parameter	**Distribution**	**Lower bound**	**Upper bound**	**Unit**
Basal Tumor Death Rate	log-uniform	0.00001	0.001	1/day
Rate of T cell exhaustion by cancer cell		0.01	1	1/day
Rate of Teff inhibition by Treg		1	0.01	1/day
Baseline PD-L1 expression on tumor/immune cells in tumor		9000	180000	molecule
Baseline PD-L1 expression on mAPCs		13000	266666	molecule
Rate of tumor vasculature growth	uniform	2.9	6.9	1/day
Max clearance rate from V1 compartment		6500	9836	microgram/hour
Half-max conc. of nab-paclitaxel for V1 clearance		24.9	58.9	microgram/liter
Max clearance rate from V1 to V2 distribution		190694	540445	microgram/hour
Half-max conc. of nab-paclitaxel for V1 to V2 distribution		2210	7910	microgram/liter
Body surface area		1.3	2.4	m^2
Peripheral compartment (V1) for nab-paclitaxel PK		13.71	17.85	liter

Peripheral compartment (V2) for nab-paclitaxel PK	1396	1935	liter
Peripheral compartment (V3) for nab-paclitaxel PK	59.8	99.1	liter
Tumor to plasma concentration ratio of nab-paclitaxel	1	2	dimensionless

REFERENCES

1. H. Wang, R. J. Sove, M. Jafarnejad, S. Rahmeh, E. M. Jaffee, V. Stearns, E. T. R. Torres, R. M. Connolly, A. S. Popel, Conducting a Virtual Clinical Trial in HER2-Negative Breast Cancer Using a Quantitative Systems Pharmacology Model With an Epigenetic Modulator and Immune Checkpoint Inhibitors. *Front Bioeng Biotechnol* **8**, 141 (2020).
2. P. Hahnfeldt, D. Panigrahy, J. Folkman, L. Hlatky, Tumor development under angiogenic signaling: a dynamical theory of tumor growth, treatment response, and postvascular dormancy. *Cancer Res* **59**, 4770-4775 (1999).
3. M. Robertson-Tessi, A. El-Kareh, A. Goriely, A mathematical model of tumor-immune interactions. *J Theor Biol* **294**, 56-73 (2012).
4. S. Mollard, J. Ciccolini, D. C. Imbs, R. El Cheikh, D. Barbolosi, S. Benzekry, Model driven optimization of antiangiogenics + cytotoxics combination: application to breast cancer mice treated with bevacizumab + paclitaxel doublet leads to reduced tumor growth and fewer metastasis. *Oncotarget* **8**, 23087-23098 (2017).
5. N. Desai, V. Trieu, Z. Yao, L. Louie, S. Ci, A. Yang, C. Tao, T. De, B. Beals, D. Dykes, P. Noker, R. Yao, E. Labao, M. Hawkins, P. Soon-Shiong, Increased antitumor activity, intratumor paclitaxel concentrations, and endothelial cell transport of cremophor-free, albumin-bound paclitaxel, ABI-007, compared with cremophor-based paclitaxel. *Clin Cancer Res* **12**, 1317-1324 (2006).
6. M. Garcia-Cremades, C. Pitou, P. W. Iversen, I. F. Troconiz, Translational Framework Predicting Tumour Response in Gemcitabine-Treated Patients with Advanced Pancreatic and Ovarian Cancer from Xenograft Studies. *AAPS J* **21**, 23 (2019).
7. E. A. Eisenhauer, P. Therasse, J. Bogaerts, L. H. Schwartz, D. Sargent, R. Ford, J. Dancey, S. Arbuck, S. Gwyther, M. Mooney, L. Rubinstein, L. Shankar, L. Dodd, R. Kaplan, D. Lacombe, J. Verweij, New response evaluation criteria in solid tumours: revised RECIST guideline (version 1.1). *Eur J Cancer* **45**, 228-247 (2009).
8. T. Torcellan, H. R. Hampton, J. Bailey, M. Tomura, R. Brink, T. Chtanova, In vivo photolabeling of tumor-infiltrating cells reveals highly regulated egress of T-cell subsets from tumors. *Proc Natl Acad Sci U S A* **114**, 5677-5682 (2017).
9. P. Autissier, C. Soulas, T. H. Burdo, K. C. Williams, Evaluation of a 12-color flow cytometry panel to study lymphocyte, monocyte, and dendritic cell subsets in humans. *Cytometry A* **77**, 410-419 (2010).

10. H. S. Robins, P. V. Campregher, S. K. Srivastava, A. Wacher, C. J. Turtle, O. Kahsai, S. R. Riddell, E. H. Warren, C. S. Carlson, Comprehensive assessment of T-cell receptor beta-chain diversity in alphabeta T cells. *Blood* **114**, 4099-4107 (2009).
11. I. Bains, R. Antia, R. Callard, A. J. Yates, Quantifying the development of the peripheral naive CD4+ T-cell pool in humans. *Blood* **113**, 5480-5487 (2009).
12. J. Yeh, J. Chun, S. Schwartz, A. Wang, E. Kern, A. A. Guth, D. Axelrod, R. Shapiro, F. Schnabel, Clinical Characteristics in Patients with Triple Negative Breast Cancer. *Int J Breast Cancer* **2017**, 1796145 (2017).
13. P. Ye, D. E. Kirschner, Reevaluation of T cell receptor excision circles as a measure of human recent thymic emigrants. *J Immunol* **168**, 4968-4979 (2002).
14. H. Zhu, R. J. Melder, L. T. Baxter, R. K. Jain, Physiologically based kinetic model of effector cell biodistribution in mammals: implications for adoptive immunotherapy. *Cancer Res* **56**, 3771-3781 (1996).
15. I. den Braber, T. Mugwagwa, N. Vrisekoop, L. Westera, R. Mogling, A. B. de Boer, N. Willems, E. H. Schrijver, G. Spierenburg, K. Gaiser, E. Mul, S. A. Otto, A. F. Ruiter, M. T. Ackermans, F. Miedema, J. A. Borghans, R. J. de Boer, K. Tesselaar, Maintenance of peripheral naive T cells is sustained by thymus output in mice but not humans. *Immunity* **36**, 288-297 (2012).
16. P. Narang, M. Chen, A. A. Sharma, K. S. Anderson, M. A. Wilson, The neoepitope landscape of breast cancer: implications for immunotherapy. *BMC Cancer* **19**, 200 (2019).
17. J. M. Marchingo, A. Kan, R. M. Sutherland, K. R. Duffy, C. J. Wellard, G. T. Belz, A. M. Lew, M. R. Dowling, S. Heinzel, P. D. Hodgkin, T cell signaling. Antigen affinity, costimulation, and cytokine inputs sum linearly to amplify T cell expansion. *Science* **346**, 1123-1127 (2014).
18. X. Chen, T. P. Hickling, P. Vicini, A mechanistic, multiscale mathematical model of immunogenicity for therapeutic proteins: part 1-theoretical model. *CPT Pharmacometrics Syst Pharmacol* **3**, e133 (2014).
19. S. Palsson, T. P. Hickling, E. L. Bradshaw-Pierce, M. Zager, K. Jooss, P. J. O'Brien, M. E. Spilker, B. O. Palsson, P. Vicini, The development of a fully-integrated immune response model (FIRM) simulator of the immune response through integration of multiple subset models. *BMC Syst Biol* **7**, 95 (2013).
20. N. G. Agrawal, J. J. Linderman, Mathematical modeling of helper T lymphocyte/antigen-presenting cell interactions: analysis of methods for modifying antigen processing and presentation. *J Theor Biol* **182**, 487-504 (1996).
21. B. Martin, C. Auffray, A. Delpoux, A. Pommier, A. Durand, C. Charvet, P. Yakonowsky, H. de Boysson, N. Bonilla, A. Audemard, T. Sparwasser, B. L. Salomon, B. Malissen, B. Lucas, Highly self-reactive naive CD4 T cells are prone to differentiate into regulatory T cells. *Nat Commun* **4**, 2209 (2013).
22. M. Jafarnejad, C. Gong, E. Gabrielson, I. H. Bartelink, P. Vicini, B. Wang, R. Narwal, L. Roskos, A. S. Popel, A Computational Model of Neoadjuvant PD-1 Inhibition in Non-Small Cell Lung Cancer. *AAPS J* **21**, 79 (2019).
23. H. Wang, O. Milberg, I. H. Bartelink, P. Vicini, B. Wang, R. Narwal, L. Roskos, C. A. Santa-Maria, A. S. Popel, In silico simulation of a clinical trial with anti-CTLA-4 and anti-PD-L1

immunotherapies in metastatic breast cancer using a systems pharmacology model. *R Soc Open Sci* **6**, 190366 (2019).

24. D. Venturoli, B. Rippe, Ficoll and dextran vs. globular proteins as probes for testing glomerular permselectivity: effects of molecular size, shape, charge, and deformability. *Am J Physiol Renal Physiol* **288**, F605-613 (2005).
25. D. G. Garlick, E. M. Renkin, Transport of large molecules from plasma to interstitial fluid and lymph in dogs. *Am J Physiol* **219**, 1595-1605 (1970).
26. F. Yuan, M. Dellian, D. Fukumura, M. Leunig, D. A. Berk, V. P. Torchilin, R. K. Jain, Vascular permeability in a human tumor xenograft: molecular size dependence and cutoff size. *Cancer Res* **55**, 3752-3756 (1995).
27. G. M. Thurber, K. Dane Wittrup, A mechanistic compartmental model for total antibody uptake in tumors. *J Theor Biol* **314**, 57-68 (2012).
28. M. Stroh, H. Winter, M. Marchand, L. Claret, S. Eppler, J. Ruppel, O. Abidoye, S. L. Teng, W. T. Lin, S. Dayog, R. Bruno, J. Jin, S. Girish, Clinical Pharmacokinetics and Pharmacodynamics of Atezolizumab in Metastatic Urothelial Carcinoma. *Clin Pharmacol Ther* **102**, 305-312 (2017).
29. X. Cheng, V. Veverka, A. Radhakrishnan, L. C. Waters, F. W. Muskett, S. H. Morgan, J. Huo, C. Yu, E. J. Evans, A. J. Leslie, M. Griffiths, C. Stubberfield, R. Griffin, A. J. Henry, A. Jansson, J. E. Ladbury, S. Ikemizu, M. D. Carr, S. J. Davis, Structure and interactions of the human programmed cell death 1 receptor. *J Biol Chem* **288**, 11771-11785 (2013).
30. M. Mkrtichyan, Y. G. Najjar, E. C. Raulfs, L. Liu, S. Langerman, G. Guittard, L. Ozbun, S. N. Khleif, B7-DC-Ig enhances vaccine effect by a novel mechanism dependent on PD-1 expression level on T cell subsets. *J Immunol* **189**, 2338-2347 (2012).
31. B. D. Harms, J. D. Kearns, S. Iadevaia, A. A. Lugovskoy, Understanding the role of cross-arm binding efficiency in the activity of monoclonal and multispecific therapeutic antibodies. *Methods* **65**, 95-104 (2014).
32. D. S. Shin, J. M. Zaretsky, H. Escuin-Ordinas, A. Garcia-Diaz, S. Hu-Lieskovan, A. Kalbasi, C. S. Grasso, W. Hugo, S. Sandoval, D. Y. Torrejon, N. Palaskas, G. A. Rodriguez, G. Parisi, A. Azhdam, B. Chmielowski, G. Cherry, E. Seja, B. Berent-Maoz, I. P. Shintaku, D. T. Le, D. M. Pardoll, L. A. Diaz, Jr., P. C. Tumeh, T. G. Graeber, R. S. Lo, B. Comin-Anduix, A. Ribas, Primary Resistance to PD-1 Blockade Mediated by JAK1/2 Mutations. *Cancer Discov* **7**, 188-201 (2017).
33. A. Jansson, E. Barnes, P. Klenerman, M. Harlen, P. Sorensen, S. J. Davis, P. Nilsson, A theoretical framework for quantitative analysis of the molecular basis of costimulation. *J Immunol* **175**, 1575-1585 (2005).
34. D. Sugiura, T. Maruhashi, I. M. Okazaki, K. Shimizu, T. K. Maeda, T. Takemoto, T. Okazaki, Restriction of PD-1 function by cis-PD-L1/CD80 interactions is required for optimal T cell responses. *Science* **364**, 558-566 (2019).
35. P. S. Linsley, S. G. Nadler, J. Bajorath, R. Peach, H. T. Leung, J. Rogers, J. Bradshaw, M. Stebbins, G. Leytze, W. Brady, et al., Binding stoichiometry of the cytotoxic T lymphocyte-associated molecule-4 (CTLA-4). A disulfide-linked homodimer binds two CD86 molecules. *J Biol Chem* **270**, 15417-15424 (1995).

36. S. Bhatia, M. Edidin, S. C. Almo, S. G. Nathenson, Different cell surface oligomeric states of B7-1 and B7-2: implications for signaling. *Proc Natl Acad Sci U S A* **102**, 15569-15574 (2005).
37. C. M. Diaz-Montero, M. L. Salem, M. I. Nishimura, E. Garrett-Mayer, D. J. Cole, A. J. Montero, Increased circulating myeloid-derived suppressor cells correlate with clinical cancer stage, metastatic tumor burden, and doxorubicin-cyclophosphamide chemotherapy. *Cancer Immunol Immunother* **58**, 49-59 (2009).
38. B. Huang, Z. Lei, J. Zhao, W. Gong, J. Liu, Z. Chen, Y. Liu, D. Li, Y. Yuan, G. M. Zhang, Z. H. Feng, CCL2/CCR2 pathway mediates recruitment of myeloid suppressor cells to cancers. *Cancer Lett* **252**, 86-92 (2007).
39. P. Dutta, M. Sarkissyan, K. Paico, Y. Wu, J. V. Vadgama, MCP-1 is overexpressed in triple-negative breast cancers and drives cancer invasiveness and metastasis. *Breast Cancer Res Treat* **170**, 477-486 (2018).
40. P. Serafini, S. Mgebroff, K. Noonan, I. Borrello, Myeloid-derived suppressor cells promote cross-tolerance in B-cell lymphoma by expanding regulatory T cells. *Cancer Res* **68**, 5439-5449 (2008).
41. N. Chen, Y. Li, Y. Ye, M. Palmisano, R. Chopra, S. Zhou, Pharmacokinetics and pharmacodynamics of nab-paclitaxel in patients with solid tumors: disposition kinetics and pharmacology distinct from solvent-based paclitaxel. *J Clin Pharmacol* **54**, 1097-1107 (2014).
42. T. Yang, M. K. Choi, F. D. Cui, S. J. Lee, S. J. Chung, C. K. Shim, D. D. Kim, Antitumor effect of paclitaxel-loaded PEGylated immunoliposomes against human breast cancer cells. *Pharm Res* **24**, 2402-2411 (2007).
43. N. V. Rajeshkumar, S. Yabuuchi, S. G. Pai, Z. Tong, S. Hou, S. Bateman, D. W. Pierce, C. Heise, D. D. Von Hoff, A. Maitra, M. Hidalgo, Superior therapeutic efficacy of nab-paclitaxel over cremophor-based paclitaxel in locally advanced and metastatic models of human pancreatic cancer. *Br J Cancer* **115**, 442-453 (2016).
44. X. Ji, Y. Lu, H. Tian, X. Meng, M. Wei, W. C. Cho, Chemoresistance mechanisms of breast cancer and their countermeasures. *Biomed Pharmacother* **114**, 108800 (2019).
45. S. S. Muerkoster, J. Lust, A. Arlt, R. Hasler, M. Witt, T. Sebens, S. Schreiber, U. R. Folsch, H. Schafer, Acquired chemoresistance in pancreatic carcinoma cells: induced secretion of IL-1beta and NO lead to inactivation of caspases. *Oncogene* **25**, 3973-3981 (2006).
46. W. Yang, J. Soares, P. Greninger, E. J. Edelman, H. Lightfoot, S. Forbes, N. Bindal, D. Beare, J. A. Smith, I. R. Thompson, S. Ramaswamy, P. A. Futreal, D. A. Haber, M. R. Stratton, C. Benes, U. McDermott, M. J. Garnett, Genomics of Drug Sensitivity in Cancer (GDSC): a resource for therapeutic biomarker discovery in cancer cells. *Nucleic Acids Res* **41**, D955-961 (2013).
47. V. Nemcova-Furstova, D. Kopperova, K. Balusikova, M. Ehrlichova, V. Brynychova, R. Vaclavikova, P. Daniel, P. Soucek, J. Kovar, Characterization of acquired paclitaxel resistance of breast cancer cells and involvement of ABC transporters. *Toxicol Appl Pharmacol* **310**, 215-228 (2016).
48. N. Gupta, P. Gupta, S. K. Srivastava, Penfluridol overcomes paclitaxel resistance in metastatic breast cancer. *Sci Rep* **9**, 5066 (2019).

49. M. Zhao, C. Lei, Y. Yang, X. Bu, H. Ma, H. Gong, J. Liu, X. Fang, Z. Hu, Q. Fang, Abraxane, the Nanoparticle Formulation of Paclitaxel Can Induce Drug Resistance by Up-Regulation of P-gp. *PLoS One* **10**, e0131429 (2015).
50. Y. Li, C. Liu, K. Tang, Y. Chen, K. Tian, Z. Feng, J. Chen, Novel multikinase inhibitor, T03 inhibits Taxolresistant breast cancer. *Mol Med Rep* **17**, 2373-2383 (2018).
51. L. D. Volk, M. J. Flister, C. M. Bivens, A. Stutzman, N. Desai, V. Trieu, S. Ran, Nab-paclitaxel efficacy in the orthotopic model of human breast cancer is significantly enhanced by concurrent anti-vascular endothelial growth factor A therapy. *Neoplasia* **10**, 613-623 (2008).
52. V. Trieu, S. Ran, N. Desai, Investigation of chemotherapy-induced tumor angiogenesis: Rationale for combination of nab-paclitaxel with anti-VEGF therapy. *Cancer Research* **67**, 4636-4636 (2007).